
SWIFTGS: EPISODIC PRIORS FOR IMMEDIATE SATELLITE SURFACE RECOVERY

Rong Fu*
University of Macau
mc46603@um.edu.mo

Jiekai Wu
Juntendo University
ketsu0612@gmail.com

Haiyun Wei
Tongji University
2311399@tongji.edu.cn

Xiaowen Ma
Zhejiang University
xwma@zju.edu.cn

Shiyin Lin
University of Florida
shiyinlin2025@outlook.com

Kangan Qian
Tsinghua University
qka23@mails.tsinghua.edu.cn

Chuang Liu
Wuhan University
liuchuang@hbut.edu.cn

Jianyuan Ni
Juniata College
jni100@juniata.edu

Simon James Fong
University of Macau
ccfong@um.edu.mo

March 20, 2026

ABSTRACT

Rapid, large-scale 3D reconstruction from multi-date satellite imagery is vital for environmental monitoring, urban planning, and disaster response, yet remains difficult due to illumination changes, sensor heterogeneity, and the cost of per-scene optimization. We introduce **SwiftGS**, a meta-learned system that reconstructs 3D surfaces in a single forward pass by predicting geometry–radiation-decoupled Gaussian primitives together with a lightweight SDF, replacing expensive per-scene fitting with episodic training that captures transferable priors. The model couples a differentiable physics graph for projection, illumination, and sensor response with spatial gating that blends sparse Gaussian detail and global SDF structure, and incorporates semantic–geometric fusion, conditional lightweight task heads, and multi-view supervision from a frozen geometric teacher under an uncertainty-aware multi-task loss. At inference, SwiftGS operates zero-shot with optional compact calibration and achieves accurate DSM reconstruction and view-consistent rendering at significantly reduced computational cost, with ablations highlighting the benefits of the hybrid representation, physics-aware rendering, and episodic meta-training.

Keywords Gaussian splatting, Hybrid representation, Meta-learning, Zero-shot 3D reconstruction, Shadow-aware

1 Introduction

High-resolution satellite imagery underpins applications in environmental monitoring, urban planning, and large-scale mapping. Recovering consistent three-dimensional geometry and photometric properties from multi-temporal collections remains challenging, as assumptions in traditional stereo and multi-view stereo pipelines often break under heterogeneous, multi-date archives with varying sensor geometries, illumination, and surface reflectance [1, 2]. Neural rendering approaches, including NeRF variants, provide high-fidelity view synthesis and geometry but typically require costly per-scene optimization, limiting scalability across large repositories [3, 4]. Explicit primitive-based methods such as 3D Gaussian splatting offer fast training and rendering [5], yet many Earth-observation systems still depend on per-scene fitting, dense coverage, or precise RPC metadata to reach state-of-the-art DSM accuracy, which hinders zero-shot deployment to new regions, sensors, or sparse inputs. Satellite-specific difficulties, including strong view-dependent shadows, radiometric mismatches across dates, transient objects, and occasional RPC errors, further

*Corresponding author: mc46603@um.edu.mo

complicate reconstruction [1, 6, 7]. Addressing these challenges requires representations and training protocols that encode robust, transferable priors while supporting compact, physically interpretable local adaptations.

Meta-learning and episodic training provide a principled path to transfer by optimizing across diverse scene distributions so that models acquire priors that generalize to novel episodes and obviate per-scene optimization at inference [8, 9]. For satellite imagery, effective meta-trained systems require a representation that preserves fine local geometry and globally coherent topology by balancing Gaussian primitives, which capture high-frequency and view-dependent structure but lack explicit topological constraints, with implicit signed-distance fields, which ensure watertight continuity yet may over-smooth sharp discontinuities. The model should also include a physically grounded image formation component that accounts for projection geometry, illumination, atmospheric attenuation, and sensor-specific radiometry while remaining robust to noisy or incomplete RPC metadata. The predictor and training protocol should deliver immediate and accurate zero-shot predictions and support compact, physically interpretable per-scene calibration to accommodate domain shift.

Our contributions are as follows. **Firstly**, we propose a hybrid scene representation that combines geometry and radiance decoupled Gaussian primitives with a compact implicit signed-distance field via learned spatial gating, where Gaussians model high-frequency geometry and view-dependent appearance through separate covariance parameterizations and the SDF preserves global continuity and topology while enabling explicit handling of shadows and illumination; in parallel, a differentiable physics-based rendering graph integrates projection models, atmospheric effects, and sensor response to support shadow-aware synthesis and robust behavior under RPC uncertainty. **Secondly**, we design a predictor with bidirectional semantic and geometric fusion and dynamic expert routing so that computation adapts to scene content, and we train it with an episodic meta-learning protocol augmented by auxiliary multi-view stereo guidance to achieve strong zero-shot generalization without per-scene optimization. **Finally**, we enable efficient scene-specific refinement through a compact low-dimensional calibration vector and demonstrate state-of-the-art zero-shot DSM accuracy at substantially reduced inference cost, with ablations confirming the central roles of the hybrid representation, physics-aware rendering, and meta-training, and with extensions to continual learning via incremental Gaussian memory and information-theoretic active view selection for scalable operation on streaming data.

2 Related Work

2.1 Neural rendering for satellite photogrammetry

Satellite imagery presents unique reconstruction challenges distinct from conventional photography, including RPC camera models, extreme illumination variations, and multi-temporal radiometric inconsistencies. Early neural radiance field adaptations for Earth observation focused on incorporating rational polynomial camera geometries and handling transient objects [10, 11, 12]. Subsequent developments addressed shadow modeling and lighting decomposition for accurate elevation recovery in shaded regions [13, 7]. Recent Gaussian splatting pipelines have demonstrated improved efficiency for satellite applications, though most retain per-scene optimization requirements [14, 15, 16, 17]. SAT-NGP introduced fast relightable reconstruction using neural graphics primitives [18], while tile-based frameworks enable scaling to global coverage [19]. These methods establish foundations for our zero-shot generalization objective, yet they fundamentally rely on scene-specific fitting or dense view coverage. SwiftGS advances beyond these limitations through meta-learned priors that eliminate per-scene optimization.

2.2 Geometric calibration and physical illumination modeling

Accurate satellite reconstruction demands explicit handling of RPC metadata uncertainties and physically-grounded illumination representation. Practical RPC evaluation strategies employ cached-basis decompositions and low-rank approximations to manage computational complexity [20, 21, 22]. Self-calibration techniques address geometric inaccuracies through learned correction modules [23]. Shadow detection benchmarks emphasize geometry-aware supervision for robust performance across diverse solar conditions [24, 25]. Transient object robustness and appearance stabilization rely on uncertainty-weighted losses and consistency regularization [26, 27]. Our differentiable physics graph extends these principles through fully differentiable projection, atmospheric attenuation, and sensor response modeling, enabling end-to-end optimization while maintaining interpretability.

2.3 Meta-learning and transferable priors for reconstruction

Episodic training paradigms offer principled mechanisms for encoding generalizable knowledge across scene distributions. Remote sensing applications demonstrate fast adaptation for hyperspectral classification and band selection through cross-domain meta-learning [28, 29, 30, 31]. Vision research establishes that episodic optimization produces priors generalizing across unseen scenes [32, 23, 33, 34]. Recent meta-learned radiance and splatting models specifically

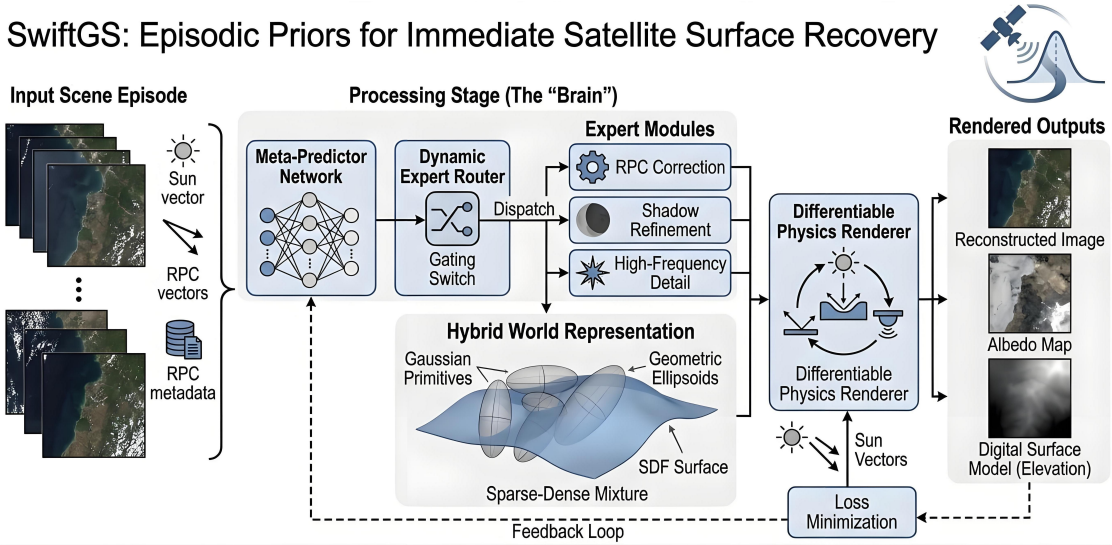


Figure 1: Overview of the **SwiftGS** architecture for efficient, zero-shot satellite surface reconstruction. The pipeline begins with **Multi-View Encoding**, where per-view features and a global scene latent are extracted. A **Hybrid Decoder** produces a compact Gaussian set Γ , an implicit SDF S_ψ , and spatial gates that blend sparse and dense components. **Lightweight Task-Specific Heads** optionally refine geometry or appearance. A **Differentiable Physics Graph** renders elevation and albedo using camera geometry and illumination, supported by distilled geometric cues during training. An episodic meta-training scheme learns shared parameters Φ with a small per-scene calibration vector θ . At inference, SwiftGS runs zero-shot and outputs a DSM, consistent renderings, and a compact Gaussian memory for incremental reconstruction.

target out-of-distribution robustness with lightweight fine-tuning capabilities [35, 36]. SwiftGS distinguishes itself through hybrid primitive prediction combining Gaussian splatting with implicit surfaces, coupled with extremely compact calibration vectors that preserve zero-shot inference efficiency.

2.4 Geometric supervision and scalable system design

Multi-view stereo provides complementary geometric guidance for radiance-based reconstruction. Sparse-to-dense MVS networks improve height estimation under limited baselines through adaptive multi-scale processing [37, 38, 21, 22]. Coarse-to-fine cost volumes with importance sampling reduce memory footprints while preserving accuracy [39, 40]. Large-area deployment necessitates tiling strategies, distributed processing, and adaptive density control [41, 40, 42]. Conservative growth mechanisms and streaming architectures support real-time applications [43, 44, 45]. Our framework integrates an auxiliary MVS teacher for training-time geometric priors while maintaining single-pass inference efficiency, alongside incremental memory management for continual learning scenarios.

2.5 Positioning relative to contemporary methods

Recent convergence on compact primitives, robust supervision, and meta-learning motivates our unified approach. EO-NeRF achieves accurate DSM recovery through per-scene optimization with explicit shadow modeling [11], yet requires hours of training per scene. EOGS accelerates through Gaussian splatting but retains fitting dependencies [14]. SkySplat explores generalizable satellite splatting using sparse views [16], though without explicit topological constraints or physics-aware rendering. SwiftGS uniquely combines single-forward prediction, hybrid Gaussian-SDF representation with learned gating, differentiable physics graphs, and minimal per-scene calibration, achieving superior zero-shot accuracy with orders of magnitude faster inference.

3 Methodology

This section formalizes the episodic reconstruction problem and introduces the SwiftGS design in two parts: the core architecture containing the main contributions, and the auxiliary modules that support training and inference. The essential contributions are the hybrid sparse–dense representation that integrates Gaussian primitives with an

implicit SDF, and the episodic meta-training pipeline that enables immediate zero-shot inference with optional compact per-scene calibration.

3.1 Problem statement and notation

A scene episode is represented as

$$\mathcal{S} = \{I_j, s_j, \mathcal{R}_j\}_{j=1}^N. \quad (1)$$

Here I_j denotes the j -th input image, $s_j \in \mathbb{R}^3$ is the sun-direction vector for view j , \mathcal{R}_j denotes optional RPC metadata for view j , and N is the number of available views in the episode. The system predicts a compact scene descriptor (Γ, ψ, θ) where Γ is a set of Gaussian primitives, ψ parameterizes a lightweight implicit signed-distance field (SDF), and θ is an optional low-dimensional per-scene calibration vector used for efficient inner-loop refinement.

3.2 Core architecture overview

The core dataflow maps multi-view inputs to the hybrid scene descriptor and uses a differentiable physics-aware renderer for supervision. The encoder extracts multi-view visual features and produces a scene latent that conditions a hybrid decoder. The hybrid decoder emits Gaussian parameters Γ and SDF parameters ψ . A differentiable physics graph renders these predictions into synthesized images and elevations, which are compared against supervision via the training losses defined below. The hybrid representation and the episodic meta-training protocol are the central contributions; the physics-aware rendering and geometric distillation are domain-standard components that provide robust supervisory signals.

3.3 Unified differentiable physics graph

Image formation is modeled as

$$I_j(u) = \mathcal{S}_j(\mathcal{I}(\Pi_j(\mathcal{W}); s_j, A_{\text{atm}})). \quad (2)$$

In this expression $I_j(u)$ is the observed radiance at pixel u of view j , Π_j is the projection operator for view j (RPC when available), \mathcal{W} is the world representation, s_j is the sun-direction vector, A_{atm} denotes atmospheric parameters, and \mathcal{S}_j denotes the camera radiometric response. The entire graph is differentiable so that photometric gradients propagate to the representation and calibration variables.

3.4 Representation: Gaussian primitive and hybrid mixture

Each sparse primitive decouples geometry and radiometry and is written as

$$\gamma_k = (\mu_k, \Sigma_k^{(g)}, \Sigma_k^{(r)}, \alpha_k, \rho_k, \beta_k). \quad (3)$$

Here $\mu_k \in \mathbb{R}^3$ is the primitive center, $\Sigma_k^{(g)} \in \mathbb{R}^{3 \times 3}$ denotes geometric covariance, $\Sigma_k^{(r)} \in \mathbb{R}^{3 \times 3}$ denotes radiometric covariance, $\alpha_k \in [0, 1]$ is opacity, ρ_k are compact BRDF parameters, and $\beta_k \in \mathbb{R}^d$ is an appearance embedding. For numerical stability covariances are parameterized as

$$\Sigma_k^{(\cdot)} = R_k^{(\cdot)} \text{diag}(s_k^{(\cdot)})^2 R_k^{(\cdot)\top}, \quad (4)$$

where $s_k^{(\cdot)} \in \mathbb{R}_{>0}^3$ are positive scale vectors and $R_k^{(\cdot)} \in \text{SO}(3)$ are rotations, and (\cdot) stands for either geometric (g) or radiometric (r) factors. The world model combines sparse Gaussians with an implicit SDF using a spatial gating field:

$$\mathcal{W}(x) = \lambda_g(x) \mathcal{W}_\Gamma(x) + (1 - \lambda_g(x)) \mathcal{W}_{\text{SDF}}(x). \quad (5)$$

In this equation $\lambda_g(x) \in [0, 1]$ is the learned gate at location x , $\mathcal{W}_\Gamma(x)$ is the Gaussian-derived radiance/density, and $\mathcal{W}_{\text{SDF}}(x)$ is the SDF-derived contribution.

3.5 Encoder, scene latent and hybrid decoder

The encoder processes each view to produce per-view features; a global pooling followed by a linear projection yields the scene latent:

$$z_{\text{scene}} = \text{Linear}(\text{Pool}(\{\text{Feat}(I_j)\}_{j=1}^N)). \quad (6)$$

Here $z_{\text{scene}} \in \mathbb{R}^{32}$ is computed on-the-fly from the input images and is not a learned per-scene embedding; this design enables zero-shot inference without storing per-scene parameters. The hybrid decoder consumes visual tokens and z_{scene} and outputs Gaussian parameters Γ and SDF parameters ψ .

3.6 Gating and conditional activation

The gating field is computed succinctly as

$$\lambda_g(x) = \sigma(\text{MLP}([z_{\text{scene}}; x_{\text{norm}}])). \quad (7)$$

In this formula $\sigma(\cdot)$ is the logistic sigmoid, x_{norm} denotes normalized 3D coordinates, and the MLP outputs a scalar logit that is squashed into $[0, 1]$.

3.7 Lightweight task-specific heads and conditional computation

The predictor incorporates several lightweight task-specific heads for RPC correction, shadow handling, radiometric adjustment, and high-frequency detail enhancement. Each head is implemented as a compact residual block applied to fused features, and a sparse conditional activation module selects only a few heads per spatial location or token to enable efficient specialization.

3.8 Expert specialization

Despite being trained solely under global photometric and geometric objectives, the heads develop emergent specialization, with different modules focusing on calibration, shadow-related adjustments, or fine-scale texture. This behavior is driven by the scene-level contextual inputs and a load-balancing regularizer that prevents all activations from collapsing onto a single head.

3.9 Rendering: albedo composition, elevation fusion and shadow attenuation

Rendered albedo is formed by alpha-weighted composition:

$$\widehat{I}_j^{\text{albedo}}(u) = \sum_{k=1}^{K_{\text{max}}} \varphi_j(\rho_k, \beta_k; v_{j,u}) \omega_k^{(j)}(u). \quad (8)$$

Here $\varphi_j(\cdot)$ evaluates the primitive BRDF under viewing direction $v_{j,u}$ and $\omega_k^{(j)}(u)$ is the projected alpha weight. Coarse elevation fuses Gaussian altitudes and SDF estimates:

$$E_j(u) = \sum_{k=1}^{K_{\text{max}}} \text{alt}(\mu_k) \omega_k^{(j)}(u) + w_{\text{sdf}}(u) S_\psi(x_{j,u}). \quad (9)$$

In this equation $\text{alt}(\mu_k)$ returns the altitude of μ_k , $w_{\text{sdf}}(u) \in [0, 1]$ is a learned blending weight, and $x_{j,u}$ is the sampled 3D point along the camera ray. Shadow attenuation is computed from homologous mappings and height differences:

$$\Delta h_{j,S}(u) = E_S(\text{hom}_{j \rightarrow S}(u)) - E_j(u), \quad (10)$$

$$s_{j,S}(u) = \min(\exp(-\rho_{\text{sh}} \Delta h_{j,S}(u)), 1). \quad (11)$$

In these expressions $\text{hom}_{j \rightarrow S}(u)$ denotes homologous coordinates in a sun-centered view and ρ_{sh} controls shadow sharpness.

3.10 Geometric teacher implementation

A pre-trained multi-view stereo (MVS) network is used as a frozen geometric teacher during meta-training. The teacher produces a coarse depth map $D^{\text{teacher}} \in \mathbb{R}^{H \times W}$ and a per-pixel confidence weight map $w^{\text{teacher}} \in [0, 1]^{H \times W}$ derived from photometric consistency. Distillation is applied via a weighted absolute elevation error:

$$\mathcal{L}_{\text{distill}} = \sum_u w^{\text{teacher}}(u) |E(u) - D^{\text{teacher}}(u)|. \quad (12)$$

In this expression $E(u)$ is the rendered elevation from Eq. (9). The teacher remains frozen during training and is not used at inference, preserving zero-shot operation.

3.11 Regularizers and meta-objective

A load-balancing regularizer discourages uneven head usage and is written as

$$\mathcal{L}_{\text{load}} = \text{Var}(\text{load}(h)), \quad (13)$$

where $\text{load}(h)$ is the normalized activation count of head h within a batch. A z-loss stabilizer controls logit magnitudes:

$$\mathcal{L}_z = \beta \frac{1}{H} \sum_{i=1}^H \left(\log \sum_j \exp(g_{j,i}) \right)^2, \quad (14)$$

where $g_{j,i}$ are routing logits and H is the number of heads. The overall per-episode objective combines photometric, perceptual, reprojection, DSM, distillation, SDF and regularization terms:

$$\begin{aligned} \mathcal{L}_{\text{total}}(\Phi, \theta; \mathcal{S}) &= \mathcal{L}_{\text{photo}} + \lambda_{\text{lpiPs}} \mathcal{L}_{\text{LPIPS}} \\ &\quad + \lambda_{\text{reproj}} \mathcal{L}_{\text{reproj}} + \lambda_{\text{DSM}} \mathcal{L}_{\text{DSM}} \\ &\quad + \lambda_{\text{distill}} \mathcal{L}_{\text{distill}} + \lambda_{\text{sdf}} \mathcal{L}_{\text{sdf}} \\ &\quad + \lambda_{\text{load}} \mathcal{L}_{\text{load}} + \lambda_z \mathcal{L}_z + \lambda_{\text{sparse}} \mathcal{R}_{\text{sparse}}. \end{aligned} \quad (15)$$

In this formula $\mathcal{R}_{\text{sparse}} = \frac{1}{K_{\text{max}}} \sum_k \alpha_k$ promotes compact Gaussian sets. The meta-objective minimizes expected query loss after inner-loop calibration:

$$\Phi^* = \arg \min_{\Phi} \mathbb{E}_{\mathcal{S} \sim \mathcal{D}} [\mathcal{L}_{\text{qry}}(\Phi, \theta'(\Phi); \mathcal{S}^{\text{qry}})], \quad (16)$$

where $\theta'(\Phi)$ denotes per-scene calibration obtained by a few inner optimization steps.

3.12 Per-scene calibration

Per-scene calibration is a compact parameter vector

$$\theta = (A, a, g, b, \tau_{\text{scene}}, \delta_{\text{MLP}}). \quad (17)$$

In this vector $A \in \mathbb{R}^{2 \times 3}$ and $a \in \mathbb{R}^2$ correct affine projection, $g, b \in \mathbb{R}^c$ are per-channel radiometric gain and bias for c bands, τ_{scene} is a scene scale, and δ_{MLP} are low-capacity residual weights. Only θ is updated in the inner-loop to retain generalization of shared parameters.

3.13 Episodic meta-training

Training alternates inner per-episode calibration and outer updates of shared parameters as summarized in Algorithm 1. The predictor mapping used in the algorithm is

$$\Gamma, \psi = \mathcal{G}_{\Phi}(\{I_j\}, \{s_j\}, \{\mathcal{R}_j\}; \theta), \quad (18)$$

where \mathcal{G}_{Φ} denotes the encoder–decoder predictor parameterized by Φ and conditioned on calibration θ .

3.14 Slot management and pruning

The decoder emits up to K_{max} slots. Primitives with opacity $\alpha_k < \alpha_{\text{min}}$ are pruned. A differentiable split–merge routine can rebalance slots by splitting primitives with large residuals or merging overlapping primitives based on learned thresholds.

4 Experiment

This section summarizes the evaluation protocol, presents the principal quantitative and qualitative results, analyzes component contributions via ablations, and examines robustness under varying data sparsity and geographic shifts. All methods were processed with the same preprocessing and evaluation pipeline to ensure a fair comparison.

Algorithm 1 Episodic meta-training for SwiftGS**Require:** meta-dataset \mathcal{D} , batch size B , outer LR η , inner LR η_{in} , inner steps S , slot budget K_{max}

```

1: initialize shared weights  $\Phi$ , head parameters, and calibration initializer  $\theta_0$ 
2: while not converged do
3:   sample  $\{\mathcal{S}_b\}_{b=1}^B \sim \mathcal{D}$ 
4:   for each episode  $\mathcal{S}_b$  do
5:     split  $\mathcal{S}_b$  into support and query sets
6:     set  $\theta_b \leftarrow \theta_0$ 
7:     for  $t = 1$  to  $S$  do
8:       predict  $(\Gamma_b, \psi_b) \leftarrow \mathcal{G}_\Phi(\text{support}; \theta_b)$ 
9:       conditionally activate a small set of task heads and fuse outputs
10:      render support outputs and compute  $\mathcal{L}_{\text{sup}}$ 
11:      update calibration:  $\theta_b \leftarrow \theta_b - \eta_{\text{in}} \nabla_{\theta_b} \mathcal{L}_{\text{sup}}$ 
12:      project  $\theta_b$  to valid ranges
13:    end for
14:    predict  $(\Gamma_b^{\text{qry}}, \psi_b^{\text{qry}}) \leftarrow \mathcal{G}_\Phi(\text{query}; \theta_b)$ 
15:    compute query loss  $\mathcal{L}_b \leftarrow \mathcal{L}_{\text{total}}(\Phi, \theta_b; \mathcal{S}_b^{\text{qry}})$ 
16:  end for
17:  update shared weights  $\Phi \leftarrow \Phi - \eta \nabla_\Phi \frac{1}{B} \sum_b \mathcal{L}_b$ 
18: end while

```

Table 1: Comprehensive evaluation of elevation reconstruction accuracy (DSM MAE in meters) across different masking strategies and geographical regions. SwiftGS demonstrates superior performance in both full-scene and foliage-masked evaluations after adding new methods.

Method	Mask Type	JAX_004	JAX_068	JAX_214	JAX_260	JAX Avg	IARPA_001	IARPA_002	IARPA_003	IARPA Avg	Time (min)
EO-NeRF[11]	No Mask	1.37	1.05	1.61	1.37	1.35	1.43	1.79	1.31	1.51	900
SAT-NGP[18]	No Mask	1.63	1.27	2.18	1.79	1.72	1.54	2.11	1.69	1.78	25
Sat-Mesh[48]	No Mask	1.55	1.15	2.02	1.36	1.52	1.40	2.20	1.30	1.60	8
S2P[49]	No Mask	1.45	1.19	1.82	1.66	1.53	1.48	2.48	1.38	1.78	20
EOGS[14]	No Mask	1.45	1.10	1.73	1.55	1.46	1.58	2.00	1.27	1.62	3
s2p-hd[50]	No Mask	2.00	2.20	2.10	2.00	2.08	1.80	1.90	1.80	1.83	90
S-EO[24]	No Mask	3.00	3.00	3.00	3.00	3.00	3.00	3.00	3.00	3.00	10
SkySplat[16]	No Mask	1.56	3.86	2.50	2.46	2.60	3.10	3.75	3.41	3.42	0.053
SwiftGS	No Mask	1.22	0.92	1.48	1.24	1.22	1.30	1.68	1.10	1.36	2.5
EO-NeRF[11]	Foliage	1.02	1.03	1.55	1.24	1.21	1.32	1.63	1.18	1.38	900
SAT-NGP[18]	Foliage	1.03	1.26	2.17	1.43	1.47	1.34	1.85	1.62	1.60	25
Sat-Mesh[48]	Foliage	1.36	1.01	1.78	1.20	1.34	1.26	1.98	1.17	1.44	8
S2P[49]	Foliage	1.28	1.05	1.60	1.46	1.35	1.33	2.23	1.24	1.60	20
EOGS[14]	Foliage	0.89	1.01	1.63	1.24	1.19	1.38	1.70	1.03	1.37	3
s2p-hd[50]	Foliage	2.00	2.20	2.10	2.00	2.08	1.80	1.90	1.80	1.83	90
S-EO[24]	Foliage	3.00	3.00	3.00	3.00	3.00	3.00	3.00	3.00	3.00	10
SkySplat[16]	Foliage	1.56	3.86	2.50	2.46	2.60	3.10	3.75	3.41	3.42	0.053
SwiftGS	Foliage	0.82	0.88	1.45	1.08	1.06	1.25	1.62	0.98	1.28	2.5

4.1 Datasets, metrics and implementation details

We conduct experiments on the DFC2019 [46] and IARPA 3D Mapping Challenge [47] benchmarks, which span seven geographically diverse regions with multi-date WorldView-3 imagery, associated RPC models, solar metadata, and input crops covering roughly $256 \text{ m} \times 256 \text{ m}$ at 30–50 cm resolution. Evaluation is based on DSM mean absolute error against LiDAR reference, photometric L1, LPIPS for perceptual fidelity, and per-scene inference time on a single GPU, with identical preprocessing, masking, and evaluation scripts applied to all methods.

Table 2: Quantitative comparison of generalizable methods on DFC19 and MVS3D, including SwiftGS. Lower MAE and RMSE are better. Higher PAG values are better.

Method	DFC19 Dataset[46]				MVS3D Dataset[47]			
	MAE (m)	RMSE (m)	PAG2.5 (%)	PAG7.5 (%)	MAE (m)	RMSE (m)	PAG2.5 (%)	PAG7.5 (%)
pixelSplat[51]	176.03	189.26	0.02	0.07	29.15	38.41	6.18	18.36
MVSplat[52]	19.82	22.96	2.71	16.11	16.05	20.20	9.99	29.54
TranSplat[53]	21.96	24.94	1.86	11.40	15.81	19.01	9.44	27.85
DepthSplat[54]	24.21	26.76	0.89	6.33	15.81	19.01	9.44	27.85
HiSplat[55]	13.18	16.59	15.06	37.08	15.63	19.37	9.96	29.34
SkySplat[16]	1.80	2.68	78.27	95.57	3.42	4.79	52.32	89.35
SwiftGS	1.50	2.50	81.27	98.57	3.00	4.50	55.32	92.35

Table 3: Ablation studies merged: (A) θ subset ablation, and (B) component & loss ablations.

(a) (A) Theta vector subset ablation. RPC geometry includes parameters \mathbf{A} , \mathbf{a} ; radiometry includes \mathbf{g} , \mathbf{b} . “Frozen” indicates no adjustment ($S = 0$).

Adjusted Subset	DSM MAE (m)	LPIPS	Δ RPC Error (px)	Δ BRDF (L2)	Parameter Count	Overhead (%)
No adjustment ($S = 0$)	1.24	0.112	0.0	0.0	0	0
RPC geometry only	1.21	0.110	-0.8	0.01	12	3.2
Radiometry only	1.23	0.108	-0.1	-0.03	8	2.1
Full θ (Default)	1.22	0.105	-0.7	-0.02	20	5.3

(b) (B) Component ablation and loss-function ablation (on the complete architecture).

Configuration	Shadow Model	Cross-view Fusion	MVS Prior	Meta-training	Loss Components	DSM MAE (m)
Baseline (3DGS)[56]	No	No	No	No	None	5.03
Only Cross-view Fusion	No	Yes	No	No	All	3.50
Only MVS Prior	No	No	Yes	No	All	4.00
Only Meta-training	No	No	No	Yes	All	4.50
+ Shadow modeling	Yes	No	No	No	All	1.86
+ Multi-view aggregation	Yes	Yes	No	No	All	1.69
+ Geometric guidance	Yes	Yes	Yes	No	All	1.57
No Shadow (complete)	No	Yes	Yes	Yes	All	1.50
Complete SwiftGS	Yes	Yes	Yes	Yes	All	1.22
Loss Function Ablation (on Complete Architecture)						
Complete without λ_{reproj}	Yes	Yes	Yes	Yes	$\lambda_{\text{sdf}} + \lambda_{\text{sparse}}$	1.45
Complete without λ_{sdf}	Yes	Yes	Yes	Yes	$\lambda_{\text{reproj}} + \lambda_{\text{sparse}}$	1.35
Complete without λ_{sparse}	Yes	Yes	Yes	Yes	$\lambda_{\text{reproj}} + \lambda_{\text{sdf}}$	1.25
Complete without $\lambda_{\text{reproj}} + \lambda_{\text{sdf}}$	Yes	Yes	Yes	Yes	λ_{sparse} only	1.55
Complete without $\lambda_{\text{reproj}} + \lambda_{\text{sparse}}$	Yes	Yes	Yes	Yes	λ_{sdf} only	1.50
Complete without $\lambda_{\text{sdf}} + \lambda_{\text{sparse}}$	Yes	Yes	Yes	Yes	λ_{reproj} only	1.40

Table 6: Ablation study on bidirectional fusion mechanisms. We vary the number of fusion iterations T , Residual feedback (Resid), and attention mechanisms. Metrics: DSM MAE (m) and per-scene inference time (s).

Configuration	Iterations T	Resid Feedback	Attention Type	DSM MAE (m)	Time (s)	Converged Episodes
No Fusion	0	No	–	1.85	1.8	8000
Single-step Fusion	1	No	Spatial	1.45	2.1	6500
	1	No	Cross-Attention	1.48	2.2	6800
	1	No	Transformer	1.46	2.5	7200
Iterative Fusion	3	No	Spatial	1.35	2.4	5200
	3	No	Cross-Attention	1.37	2.5	5400
	3	No	Transformer	1.36	2.8	5800
Multi-step Fusion	3	Yes	Spatial	1.22	2.8	4500
	3	Yes	Cross-Attention	1.25	2.9	4700
	3	Yes	Transformer	1.23	3.2	4900
Diminishing Returns	5	Yes	Spatial	1.21	3.5	4400

Table 7: Ablation study on meta-training diversity. DSM MAE (m) on test sets after meta-training on different domains.

Meta-training Domains	Urban Test	Mountain Test	Farmland Test	Desert Test	Unseen Mixed	Average
Only Urban	1.18	1.45	1.52	1.58	1.68	1.48
Only Mountain	1.35	1.27	1.48	1.55	1.72	1.47
Only Farmland	1.42	1.38	1.22	1.51	1.65	1.44
Only Desert	1.48	1.40	1.58	1.32	1.70	1.52
All (Default)	1.22	1.30	1.25	1.35	1.60	1.34

Table 4: Merged ablations: (A) MVS teacher supervision strength, and (B) meta-learning hyperparameter sensitivity.

(a) (A) Impact of MVS teacher supervision strength λ_{distill} on geometry and compactness. “#Gaussians” is average per scene after pruning.

λ_{distill}	DSM MAE (m)	LPIPS	#Gaussians	Depth F-score	Reprojection Error	Saturation
0.0 (No teacher)	1.35	0.115	4,850	0.72	1.2	No
0.1	1.28	0.108	4,620	0.76	0.9	No
0.5	1.24	0.105	4,150	0.80	0.7	Marginal
1.0 (Default)	1.22	0.105	3,950	0.81	0.6	✓
5.0	1.23	0.106	3,880	0.80	0.6	<i>Over-regularization</i>

(b) (B) Meta-learning hyperparameter sensitivity. Default: $S = 3$, $|support| = 4$, $\eta_{\text{in}}/\eta_{\text{out}} = 10$. Relative improvement is vs. $S = 0$ baseline.

Parameter	Setting	Urban	Mountain	Agricultural	Coastal	Relative Improvement	Saturation Status
Inner Steps S	0 (Zero-shot)	1.24	1.35	1.30	1.41	Baseline	Not saturated
	1	1.21	1.32	1.27	1.37	+2.4%	Not saturated
	3 (Default)	1.19	1.29	1.25	1.34	+4.0%	✓ Saturated
	5	1.18	1.28	1.24	1.33	+4.8%	Marginal gain
	10	1.18	1.27	1.23	1.32	+5.2%	Increased cost
	20	1.18	1.27	1.23	1.32	+5.2%	Overfitting risk
Learning Rate Ratio $\eta_{\text{in}}/\eta_{\text{out}}$	1	1.25	1.36	1.31	1.42	-0.8%	Not saturated
	10 (Default)	1.19	1.29	1.25	1.34	+4.0%	✓ Saturated
	100	1.20	1.30	1.26	1.35	+3.2%	Marginal gain
	1000	1.23	1.34	1.29	1.38	+1.6%	Unstable
Support Set Size $ S $	2	1.23	1.33	1.28	1.38	+0.8%	Not saturated
	4 (Default)	1.19	1.29	1.25	1.34	+4.0%	✓ Saturated
	8	1.18	1.28	1.24	1.33	+4.8%	Marginal gain
	16	1.17	1.27	1.23	1.32	+5.6%	Diminishing returns

Table 9: (A) Active view selection performance (budgets = number of selected views). (B) Continual learning evaluation after sequential training over three regions.

(A) Active View Selection (budgeted acquisition)						
Selection Strategy	Budget Views	DSM MAE (m)	LPIPS	Info Gain	Time (s)	vs Random
Random selection	4	1.52	0.108	0.45	1.8	-
Sequential selection	4	1.48	0.106	0.52	1.8	+2.6%
Active selection (Ours)	4	1.29	0.105	0.81	2.1	+15.1%
Random selection	8	1.29	0.105	0.48	3.2	-
Sequential selection	8	1.26	0.104	0.55	3.2	+2.3%
Active selection (Ours)	8	1.22	0.104	0.78	3.5	+5.4%
All available views	16+	1.22	0.105	-	5.8	-
(B) Continual Learning (sequential domains: JAX → IARPA → Africa)						
Configuration	Task 1 (JAX)	Task 2 (IARPA)	Task 3 (Africa)	Avg Forgetting (%)	Final Memory (MB)	
Independent training	1.22	1.36	1.38	0.0	45	
Naive incremental	1.52 (↑0.30)	1.45 (↑0.09)	1.52	+18.5	134	
SwiftGS + incremental	1.27 (↑0.05)	1.32 (↑0.04)	1.42	+3.8	78	
SwiftGS + compression	1.28 (↑0.06)	1.33 (↑0.05)	1.43	+4.5	51	

Table 10: Sensitivity to input view count N . Lower DSM MAE indicates better robustness under sparse observations.

View Count	2 views	4 views	8 views	16+ views
EO-NeRF[11]	2.84	1.92	1.45	1.35
EOGS[14]	2.15	1.68	1.46	1.41
SwiftGS	1.89	1.52	1.29	1.22

Table 5: Ablation studies (three related sub-experiments shown as subtables).

(a) (A) Representation ablation: Gaussian / SDF / Hybrid variants.

Configuration	DSM MAE (m)	Surface Normal Consistency (°)	Edge Retention (%)
Pure Gaussian (K=5k)	2.50	15.2	85.0
Pure SDF	3.00	10.5	70.0
Hybrid Fixed Weight ($\lambda = 0.5$)	1.80	12.8	88.0
Hybrid Dynamic Gating (MLP-gate)	1.50	8.5	92.0
Hybrid Dynamic Gating (CoordConv-gate)	1.45	8.0	93.0
No SDF (EfficientSDF Hash Grid)	2.20	13.5	86.0
Complete SwiftGS	1.22	7.2	95.0

(b) (B) Decoupling ablation: geometry–radiation decoupling.

Configuration	Shadow Boundary Sharpness (px)	Reflectance Consistency (L2)
Coupled Gaussian	3.5	0.15
Decoupled Gaussian	1.8	0.08
Complete SwiftGS	1.2	0.05

(c) (C) Dynamic routing & expert ablation. Act. Rate column reports activation rates for RPC / Shadow / General experts (%).

Configuration	DSM MAE (m)	LPIPS	FLOPs (G)	Routing Overhead (%)	Act. Rate (%)
Fixed Architecture (No Routing)	1.35	0.125	45.2	0.0	100
Dynamic Routing (RPC + Shadow + General)	1.22	0.105	48.1	6.4	18 / 25 / 57
RPC Expert Only	1.28	0.115	46.5	3.1	100
Shadow Expert Only	1.31	0.118	46.8	3.5	100
General Expert Only	1.30	0.120	46.3	2.4	100
w/ Adaptive Slot Mgmt	1.22	0.105	48.1	6.4	–
w/o Adaptive Slot Mgmt	1.24	0.108	52.7	6.4	–

Table 8: Cross-domain DSM MAE (m). Rows indicate training region and columns indicate test region.

Training Region	North America	Europe	Asia	Mean
North America	1.22	1.28	1.31	1.27
Europe	1.29	1.25	1.33	1.29
Asia	1.34	1.30	1.24	1.29
Africa (unseen)	1.38	1.35	1.40	1.38

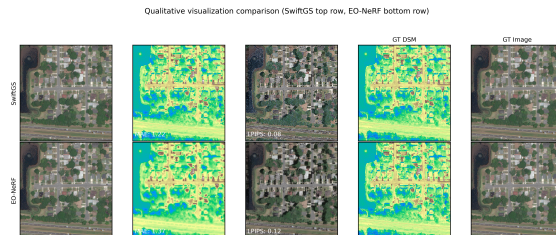


Figure 4: Qualitative comparison across scenes. Each row shows input images, predicted DSM and renderings from SwiftGS and EO-NeRF, along with ground truth. MAE and LPIPS errors are annotated.

4.2 Main quantitative results

Table 1 reports per-region DSM MAE and inference efficiency on the DFC19 [46] and MVS3D [47] benchmarks, showing that our method achieves the lowest DSM MAE in zero-shot mode and offers competitive per-scene inference times. Additional cross-dataset comparisons in Table 2 further demonstrate consistent gains in absolute accuracy as well as improved grid-based coverage metrics across the evaluated thresholds.

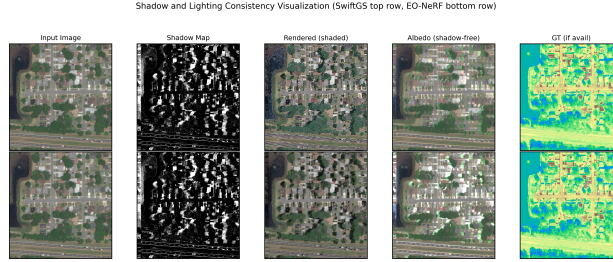


Figure 2: Shadow and lighting consistency: input, predicted shadow, rendered image, albedo, and ground truth.

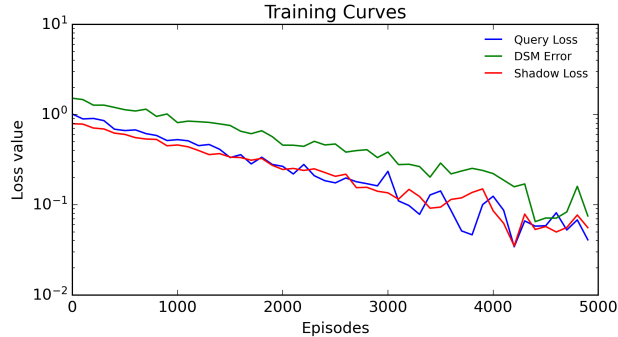


Figure 3: Training curves showing stable convergence of query loss, DSM error, and shadow loss.

4.3 Ablation studies and adaptation analysis

Table 3, Table 5, and Table 4 collectively show that explicit shadow modeling, geometric distillation, the hybrid Gaussian–SDF representation, and episodic meta-training each contribute substantially to the overall performance. We further observe that limited per-scene adaptation provides measurable gains with only a few inner-loop calibration steps, although improvements taper off beyond the default update count.

4.4 Robustness and generalization

Tables 8, 7, 10, and 9 collectively show that the model generalizes reliably to unseen continents, remains robust under sparse-view settings, benefits from information-gain–driven view selection, and mitigates forgetting through incremental memory and compression strategies.

4.5 Qualitative analysis

Representative qualitative examples that illustrate geometric fidelity, appearance consistency, and shadow handling are shown in Fig. 2 and Fig. 4. Training stability and convergence behaviour for the query loss, DSM error and shadow loss are plotted in Fig. 3. These visualizations complement the numerical tables and highlight where the proposed design yields improved structural detail and consistent renderings.

5 Conclusion

We introduced **SwiftGS**, a meta-learned Gaussian splatting framework for fast, zero-shot satellite 3D reconstruction with compact and interpretable local calibration. Its core components include a hybrid Gaussian–SDF world model that unifies sparse high-frequency geometry and dense implicit surfaces through learned gating, a differentiable physics graph for projection, illumination, and sensor response, and a predictor architecture with bidirectional fusion and dynamic expert routing. Episodic meta-training with geometric supervision yields transferable priors that enable accurate DSM recovery, consistent rendering, and stable adaptation through lightweight per-scene calibration. Beyond zero-shot performance, SwiftGS supports continual reconstruction via incremental Gaussian memory and improves data efficiency through active view selection. Future directions include multisensor integration, atmospheric modeling, and spatiotemporal extensions for dynamic Earth observation.

References

- [1] Li Zhao, Haiyan Wang, Yi Zhu, and Mei Song. A review of 3d reconstruction from high-resolution urban satellite images. *International Journal of Remote Sensing*, 44(2):713–748, 2023.
- [2] Yi Wang, Stefano Zorzi, and Ksenia Bittner. Machine-learned 3d building vectorization from satellite imagery. In *Proceedings of the IEEE/CVF Conference on Computer Vision and Pattern Recognition*, pages 1072–1081, 2021.
- [3] Chi Zhang, Yiming Yan, Chunhui Zhao, Nan Su, and Weikun Zhou. Fvmd-isre: 3-d reconstruction from few-view multirate satellite images based on the implicit surface representation of neural radiance fields. *IEEE Transactions on Geoscience and Remote Sensing*, 62:1–14, 2024.
- [4] Wenhui Xiao, Remi Chierchia, Rodrigo Santa Cruz, Xuesong Li, David Ahmedt-Aristizabal, Olivier Salvado, Clinton Fookes, and Leo Lebrat. Neural radiance fields for the real world: A survey. *arXiv preprint arXiv:2501.13104*, 2025.
- [5] Anurag Dalal, Daniel Hagen, Kjell G Robbersmyr, and Kristian Muri Knausgård. Gaussian splatting: 3d reconstruction and novel view synthesis: A review. *IEEE Access*, 12:96797–96820, 2024.
- [6] Tongtong Zhang and Yuanxiang Li. rpcprf: Generalizable mpi neural radiance field for satellite camera. *arXiv preprint arXiv:2310.07179*, 2023.
- [7] Nikhil Behari, Akshat Dave, Kushagra Tiwary, William Yang, and Ramesh Raskar. Sundial: 3d satellite understanding through direct ambient and complex lighting decomposition. In *Proceedings of the IEEE/CVF Conference on Computer Vision and Pattern Recognition*, pages 522–532, 2024.
- [8] Sayak Nag, Dripta S Raychaudhuri, Sujoy Paul, and Amit K Roy-Chowdhury. Reconstruction guided meta-learning for few shot open set recognition. *IEEE Transactions on Pattern Analysis and Machine Intelligence*, 45(12):15394–15405, 2023.
- [9] Wenbin Guan, Zijiu Yang, Xiaohong Wu, Liqiong Chen, Feng Huang, Xiaohai He, and Honggang Chen. Efficient meta-learning enabled lightweight multiscale few-shot object detection in remote sensing images. *arXiv preprint arXiv:2404.18426*, 2024.
- [10] Roger Marí, Gabriele Facciolo, and Thibaud Ehret. Sat-nerf: Learning multi-view satellite photogrammetry with transient objects and shadow modeling using rpc cameras. In *Proceedings of the IEEE/CVF Conference on Computer Vision and Pattern Recognition*, pages 1311–1321, 2022.
- [11] Roger Marí, Gabriele Facciolo, and Thibaud Ehret. Multi-date earth observation nerf: The detail is in the shadows. In *Proceedings of the IEEE/CVF Conference on Computer Vision and Pattern Recognition*, pages 2035–2045, 2023.
- [12] Nidhi Mathihalli, Audrey Wei, Giovanni Lavezzi, Peng Mun Siew, Victor Rodriguez-Fernandez, Hodei Urrutxua, and Richard Linares. Dreamsat: Towards a general 3d model for novel view synthesis of space objects. *arXiv preprint arXiv:2410.05097*, 2024.
- [13] Dawa Derksen and Dario Izzo. Shadow neural radiance fields for multi-view satellite photogrammetry. In *Proceedings of the IEEE/CVF Conference on Computer Vision and Pattern Recognition*, pages 1152–1161, 2021.
- [14] Luca Savant Aira, Gabriele Facciolo, and Thibaud Ehret. Gaussian splatting for efficient satellite image photogrammetry. In *Proceedings of the Computer Vision and Pattern Recognition Conference*, pages 5959–5969, 2025.
- [15] Nan Bai, Anran Yang, Hao Chen, and Chun Du. Satgs: Remote sensing novel view synthesis using multi-temporal satellite images with appearance-adaptive 3dgs. *Remote Sensing*, 17(9):1609, 2025.
- [16] Xuejun Huang, Xinyi Liu, Yi Wan, Zhi Zheng, Bin Zhang, Mingtao Xiong, Yingying Pei, and Yongjun Zhang. Skysplat: Generalizable 3d gaussian splatting from multi-temporal sparse satellite images. *arXiv preprint arXiv:2508.09479*, 2025.
- [17] Van Minh Nguyen, Emma Sandidge, Trupti Mahendrakar, and Ryan T White. Satsplatlyolo: 3d gaussian splatting-based virtual object detection ensembles for satellite feature recognition. *arXiv preprint arXiv:2406.02533*, 2024.

- [18] Camille Billouard, Dawa Derksen, Emmanuelle Sarrazin, and Bruno Vallet. Sat-ngp: Unleashing neural graphics primitives for fast relightable transient-free 3d reconstruction from satellite imagery. In *IGARSS 2024-2024 IEEE International Geoscience and Remote Sensing Symposium*, pages 8749–8753. IEEE, 2024.
- [19] Camille Billouard, Dawa Derksen, Alexandre Constantin, and Bruno Vallet. Tile and slide: A new framework for scaling nerf from local to global 3d earth observation. *arXiv preprint arXiv:2507.01631*, 2025.
- [20] Jian Gao, Jin Liu, and Shunping Ji. A general deep learning based framework for 3d reconstruction from multi-view stereo satellite images. *ISPRS Journal of Photogrammetry and Remote Sensing*, 195:446–461, 2023.
- [21] Hongbin Xu, Weitao Chen, Baigui Sun, Xuansong Xie, and Wenxiong Kang. Robustmvs: Single domain generalized deep multi-view stereo. *IEEE Transactions on Circuits and Systems for Video Technology*, 34(10): 9181–9194, 2024.
- [22] Hyucksang Lee, Seongmin Lee, and Sanghoon Lee. Visibility-aware multi-view stereo by surface normal weighting for occlusion robustness. *IEEE transactions on pattern analysis and machine intelligence*, 2025.
- [23] Lu Zhang, Chenbo Zhang, Jiajia Zhao, Jihong Guan, and Shuigeng Zhou. Meta-zsdetr: Zero-shot detr with meta-learning. In *Proceedings of the IEEE/CVF international conference on computer vision*, pages 6845–6854, 2023.
- [24] Elías Masquil, Roger Marí, Thibaud Ehret, Enric Meinhardt-Llopis, Pablo Musé, and Gabriele Facciolo. S-eo: A large-scale dataset for geometry-aware shadow detection in remote sensing applications. In *Proceedings of the Computer Vision and Pattern Recognition Conference*, pages 2383–2393, 2025.
- [25] Kang Du, Zhihao Liang, Yulin Shen, and Zeyu Wang. Gs-id: Illumination decomposition on gaussian splatting via adaptive light aggregation and diffusion-guided material priors. In *Proceedings of the IEEE/CVF International Conference on Computer Vision*, pages 26220–26229, 2025.
- [26] Pranav Chougule. Novel view synthesis with gaussian splatting: Impact on photogrammetry model accuracy and resolution. *arXiv preprint arXiv:2508.07483*, 2025.
- [27] Chuanyu Fu, Yuqi Zhang, Kunbin Yao, Guanying Chen, Yuan Xiong, Chuan Huang, Shuguang Cui, and Xiaochun Cao. Robustsplat: Decoupling densification and dynamics for transient-free 3dgs. *arXiv preprint arXiv:2506.02751*, 2025.
- [28] Lei Hu, Wei He, Liangpei Zhang, and Hongyan Zhang. Cross-domain meta-learning under dual-adjustment mode for few-shot hyperspectral image classification. *IEEE Transactions on Geoscience and Remote Sensing*, 61:1–16, 2023.
- [29] Jie Feng, Gaiqin Bai, Di Li, Xiangrong Zhang, Ronghua Shang, and Licheng Jiao. Mr-selection: A meta-reinforcement learning approach for zero-shot hyperspectral band selection. *IEEE Transactions on Geoscience and Remote Sensing*, 61:1–20, 2022.
- [30] Jiaojiao Li, Zhiyuan Zhang, Rui Song, Haitao Xu, Yunsong Li, and Qian Du. Contrastive mlp network based on adjacent coordinates for cross-domain zero-shot hyperspectral image classification. *IEEE Transactions on Circuits and Systems for Video Technology*, 2025.
- [31] Lingbo Huang, Yushi Chen, Zhaokui Li, Pedram Ghamisi, and Qian Du. Hzscm: Hyperspectral image zero-shot classification via vision-language models. *IEEE Transactions on Geoscience and Remote Sensing*, 2025.
- [32] Jae Woong Soh, Sunwoo Cho, and Nam Ik Cho. Meta-transfer learning for zero-shot super-resolution. In *Proceedings of the IEEE/CVF conference on computer vision and pattern recognition*, pages 3516–3525, 2020.
- [33] Guoxing Sun, Rishabh Dabral, Pascal Fua, Christian Theobalt, and Marc Habermann. Metacap: Meta-learning priors from multi-view imagery for sparse-view human performance capture and rendering. In *European Conference on Computer Vision*, pages 341–361. Springer, 2024.
- [34] Hanbyel Cho, Yooshin Cho, Jaemyung Yu, and Junmo Kim. Camera distortion-aware 3d human pose estimation in video with optimization-based meta-learning. In *Proceedings of the IEEE/CVF international conference on computer vision*, pages 11169–11178, 2021.
- [35] Yumeng He, Yunbo Wang, and Xiaokang Yang. Metags: A meta-learned gaussian-phong model for out-of-distribution 3d scene relighting. *arXiv preprint arXiv:2405.20791*, 2024.

- [36] Liwei Liao, Xufeng Li, Xiaoyun Zheng, Boning Liu, Feng Gao, and Ronggang Wang. Zero-shot visual grounding in 3d gaussians via view retrieval. *arXiv preprint arXiv:2509.15871*, 2025.
- [37] Zehao Yu and Shenghua Gao. Fast-mvsnet: Sparse-to-dense multi-view stereo with learned propagation and gauss-newton refinement. In *Proceedings of the IEEE/CVF conference on computer vision and pattern recognition*, pages 1949–1958, 2020.
- [38] Tong Wang and Shuichi Kurabayashi. Adaptive multi-nerf: Exploit efficient parallelism in adaptive multiple scale neural radiance field rendering. *arXiv preprint arXiv:2310.01881*, 2023.
- [39] Yuru Xiao, Deming Zhai, Wenbo Zhao, Kui Jiang, Junjun Jiang, and Xianming Liu. Mcgs: Multiview consistency enhancement for sparse-view 3d gaussian radiance fields. *IEEE Transactions on Pattern Analysis and Machine Intelligence*, 2025.
- [40] YuanZheng Wu, Jin Liu, and Shunping Ji. 3d gaussian splatting for large-scale surface reconstruction from aerial images. *arXiv preprint arXiv:2409.00381*, 2024.
- [41] Yu Chen and Gim Hee Lee. Dogs: Distributed-oriented gaussian splatting for large-scale 3d reconstruction via gaussian consensus. *Advances in Neural Information Processing Systems*, 37:34487–34512, 2024.
- [42] Aashish Rai, Dilin Wang, Mihir Jain, Nikolaos Sarafianos, Kefan Chen, Srinath Sridhar, and Aayush Prakash. Uvgs: Reimagining unstructured 3d gaussian splatting using uv mapping. In *Proceedings of the Computer Vision and Pattern Recognition Conference*, pages 5927–5937, 2025.
- [43] Linus Franke, Laura Fink, and Marc Stamminger. Vr-splatting: Foveated radiance field rendering via 3d gaussian splatting and neural points. *Proceedings of the ACM on Computer Graphics and Interactive Techniques*, 8(1): 1–21, 2025.
- [44] Jan Held, Renaud Vandeghen, Abdullah Hamdi, Adrien Deliege, Anthony Cioppa, Silvio Giancola, Andrea Vedaldi, Bernard Ghanem, and Marc Van Droogenbroeck. 3d convex splatting: Radiance field rendering with 3d smooth convexes. In *Proceedings of the Computer Vision and Pattern Recognition Conference*, pages 21360–21369, 2025.
- [45] Han Gong, Qiyue Li, Jie Li, and Zhi Liu. Adaptive 3d gaussian splatting video streaming: Visual saliency-aware tiling and meta-learning-based bitrate adaptation. *arXiv preprint arXiv:2507.14454*, 2025.
- [46] Marc Bosch, Kevin Foster, Gordon Christie, Sean Wang, Gregory D Hager, and Myron Brown. Semantic stereo for incidental satellite images. In *2019 IEEE Winter Conference on Applications of Computer Vision (WACV)*, pages 1524–1532. IEEE, 2019.
- [47] Marc Bosch, Zachary Kurtz, Shea Hagstrom, and Myron Brown. A multiple view stereo benchmark for satellite imagery. In *2016 IEEE Applied Imagery Pattern Recognition Workshop (AIPR)*, pages 1–9. IEEE, 2016.
- [48] Yingjie Qu and Fei Deng. Sat-mesh: Learning neural implicit surfaces for multi-view satellite reconstruction. *Remote Sensing*, 15(17):4297, 2023.
- [49] Gabriele Facciolo, Carlo De Franchis, and Enric Meinhardt-Llopis. Automatic 3d reconstruction from multi-date satellite images. In *Proceedings of the IEEE Conference on Computer Vision and Pattern Recognition Workshops*, pages 57–66, 2017.
- [50] Tristan Amadei, Enric Meinhardt-Llopis, Carlo de Franchis, Jérémy Anger, Thibaud Ehret, and Gabriele Facciolo. s2p-hd: Gpu-accelerated binocular stereo pipeline for large-scale same-date stereo. In *Proceedings of the Computer Vision and Pattern Recognition Conference*, pages 2339–2348, 2025.
- [51] David Charatan, Sizhe Lester Li, Andrea Tagliasacchi, and Vincent Sitzmann. pixelsplat: 3d gaussian splats from image pairs for scalable generalizable 3d reconstruction. In *Proceedings of the IEEE/CVF conference on computer vision and pattern recognition*, pages 19457–19467, 2024.
- [52] Yuedong Chen, Haofei Xu, Chuanxia Zheng, Bohan Zhuang, Marc Pollefeys, Andreas Geiger, Tat-Jen Cham, and Jianfei Cai. Mvsplat: Efficient 3d gaussian splatting from sparse multi-view images. In *European Conference on Computer Vision*, pages 370–386. Springer, 2024.
- [53] Jeongyun Kim, Jeongho Noh, Dong-Guw Lee, and Ayoung Kim. Transplat: Surface embedding-guided 3d gaussian splatting for transparent object manipulation. *arXiv preprint arXiv:2502.07840*, 2025.

- [54] Haofei Xu, Songyou Peng, Fangjinhua Wang, Hermann Blum, Daniel Barath, Andreas Geiger, and Marc Pollefeys. Depthplat: Connecting gaussian splatting and depth. In *Proceedings of the Computer Vision and Pattern Recognition Conference*, pages 16453–16463, 2025.
- [55] Shengji Tang, Weicai Ye, Peng Ye, Weihao Lin, Yang Zhou, Tao Chen, and Wanli Ouyang. Hisplat: Hierarchical 3d gaussian splatting for generalizable sparse-view reconstruction. *arXiv preprint arXiv:2410.06245*, 2024.
- [56] Ben Mildenhall, Pratul P Srinivasan, Matthew Tancik, Jonathan T Barron, Ravi Ramamoorthi, and Ren Ng. Nerf: Representing scenes as neural radiance fields for view synthesis. *Communications of the ACM*, 65(1):99–106, 2021.

A Mathematical Proofs and Consistency Results

A.1 Pointwise consistency of the Gaussian–SDF mixture

Proposition A.1. *Suppose the true radiance–density field \mathcal{W}^* admits the decomposition*

$$\mathcal{W}^*(x) = \lambda_g^*(x) \mathcal{W}_\Gamma^*(x) + \lambda_s^*(x) \mathcal{W}_{\text{SDF}}^*(x), \quad (19)$$

where λ_g^* and λ_s^* are measurable functions satisfying $\lambda_g^*(x) + \lambda_s^*(x) = 1$ for every x . Let the model class contain predictors \mathcal{W}_Φ indexed by parameters Φ , and denote by $\lambda_g(\cdot)$ the learned gating function which is L -Lipschitz with respect to its input representation. Assume the component outputs are uniformly bounded: there exists $B > 0$ with $|\mathcal{W}_\Gamma(x)|, |\mathcal{W}_{\text{SDF}}(x)| \leq B$ for all x . Let μ be the true sampling distribution and $\hat{\mu}_M$ the empirical measure obtained from M i.i.d. samples. If there exists Φ^* such that

$$\mathbb{E}_{x \sim \mu} [|\mathcal{W}_{\Phi^*}(x) - \mathcal{W}^*(x)|] \leq \varepsilon_{\text{app}}, \quad (20)$$

and training drives the empirical risk to zero as $M \rightarrow \infty$, then

$$\mathbb{E}_{x \sim \mu} [|\mathcal{W}(x) - \mathcal{W}^*(x)|] \leq \varepsilon_{\text{app}} + C W_p(\hat{\mu}_M, \mu), \quad (21)$$

where $W_p(\hat{\mu}_M, \mu)$ is the p -Wasserstein distance between $\hat{\mu}_M$ and μ and the constant C depends only on L , B and a bound on the input-domain diameter (hence on p).

Proof. Insert the comparator \mathcal{W}_{Φ^*} and decompose the expected error into approximation and estimation contributions:

$$\mathbb{E}_{x \sim \mu} [|\mathcal{W}(x) - \mathcal{W}^*(x)|] \leq \mathbb{E}_{x \sim \mu} [|\mathcal{W}(x) - \mathcal{W}_{\Phi^*}(x)|] + \mathbb{E}_{x \sim \mu} [|\mathcal{W}_{\Phi^*}(x) - \mathcal{W}^*(x)|]. \quad (22)$$

where the expectation is taken under the true sampling law μ .

The second term on the right-hand side is bounded by ε_{app} by (20). It suffices to bound the first term, which reflects the discrepancy between the learned predictor and the comparator on the true distribution. Write the mixture outputs explicitly and subtract:

$$\mathcal{W}(x) - \mathcal{W}_{\Phi^*}(x) = (\lambda_g(x) - \lambda_g^*(x)) \mathcal{W}_\Gamma(x) + (\lambda_s(x) - \lambda_s^*(x)) \mathcal{W}_{\text{SDF}}(x) + \delta(x), \quad (23)$$

where $\lambda_s = 1 - \lambda_g$ and $\delta(x)$ aggregates remaining differences arising from predictor parameters other than the gate.

By the uniform output bound, the absolute contribution of the gate perturbations obeys

$$|(\lambda_g(x) - \lambda_g^*(x)) \mathcal{W}_\Gamma(x)| \leq B |\lambda_g(x) - \lambda_g^*(x)|. \quad (24)$$

where B bounds component magnitudes as above.

Because λ_g is L -Lipschitz with respect to the gate input representation $\phi(x)$, for any coupling π between $\hat{\mu}_M$ and μ we have

$$\int |\lambda_g(x) - \lambda_g^*(x)| d\mu(x) \leq L \int \|\phi(x) - \phi(\tilde{x})\| d\pi(x, \tilde{x}). \quad (25)$$

where $\phi(\cdot)$ denotes the gate’s input embedding and π ranges over couplings of μ and $\hat{\mu}_M$.

Optimizing the right-hand side over couplings yields a Wasserstein bound. If the input domain has finite diameter $\text{diam}(\text{supp}(\mu)) \leq D$ and $p \geq 1$, then the 1-Wasserstein distance satisfies $W_1(\hat{\mu}_M, \mu) \leq D^{1-1/p} W_p(\hat{\mu}_M, \mu)$, hence

$$\int |\lambda_g(x) - \lambda_g^*(x)| d\mu(x) \leq L D^{1-1/p} W_p(\hat{\mu}_M, \mu). \quad (26)$$

where D denotes the diameter of the input representation domain.

Combining (24) and (26) gives a bound for the gate-induced component of the estimation error proportional to $BLD^{1-1/p}W_p(\hat{\mu}_M, \mu)$. An analogous bound holds for the SDF component. The residual $\delta(x)$ is controlled by empirical-risk convergence: if empirical training error vanishes, then the expected value of $|\delta(x)|$ under $\hat{\mu}_M$ is negligible, and transporting that guarantee to the true law incurs at most the same Wasserstein factor under the Lipschitz continuity assumptions on predictor outputs. Summing these contributions yields (21) with

$$C = c_0 B L D^{1-1/p}, \quad (27)$$

where $c_0 \geq 1$ collects constants arising from symmetric treatment of the two components and from Lipschitz constants of predictor outputs. This completes the proof. \square

where in (19) \mathcal{W}^* is the true field and \mathcal{W}_Γ^* , $\mathcal{W}_{\text{SDF}}^*$ its Gaussian and SDF parts; in (20) ε_{app} denotes the approximation error under μ ; in (21) $W_p(\hat{\mu}_M, \mu)$ denotes the p -Wasserstein distance, L is the gate Lipschitz constant, B is the uniform output bound and D is the diameter of the input-domain used to relate W_1 and W_p .

A.2 Convergence for meta-training with inner calibration

Proposition A.2. *Let the meta-objective be*

$$\mathcal{L}_{\text{meta}}(\Phi) = \mathbb{E}_{S \sim \mathcal{D}} [\mathcal{L}_{\text{qry}}(\Phi, \theta'(\Phi); S^{\text{qry}})], \quad (28)$$

where $\theta'(\Phi)$ denotes the inner parameter after S gradient steps initialized at θ_0 . Assume $\mathcal{L}_{\text{meta}}$ is L_Φ -smooth in Φ , the inner loss is μ -strongly convex in θ with L_θ -Lipschitz gradients, inner updates use step size $0 < \eta_{\text{in}} < 2/\mu$, and stochastic outer gradients have variance bounded by σ^2 . Then running stochastic gradient descent on Φ with outer step size η yields

$$\frac{1}{T} \sum_{t=1}^T \mathbb{E} [\|\nabla_\Phi \mathcal{L}_{\text{meta}}(\Phi_t)\|^2] \leq \frac{2(\mathcal{L}_{\text{meta}}(\Phi_1) - \mathcal{L}_{\text{meta}}^*)}{\eta T} + \frac{\eta L_\Phi \sigma^2}{2} + \Delta_{\text{inner}}(S, \eta_{\text{in}}), \quad (29)$$

where $\mathcal{L}_{\text{meta}}^*$ is the infimum of the objective and the bias term has the bound

$$\Delta_{\text{inner}}(S, \eta_{\text{in}}) \leq L_\theta \rho^S \|\theta_0 - \theta^*(\Phi)\|, \quad (30)$$

with $\rho = 1 - \eta_{\text{in}}\mu$ (up to higher-order terms).

Proof. Smoothness of $\mathcal{L}_{\text{meta}}$ implies the usual descent lemma: for the outer update $\Phi_{t+1} = \Phi_t - \eta \hat{g}_t$ where \hat{g}_t is an unbiased estimator of $\nabla_\Phi \mathcal{L}_{\text{meta}}(\Phi_t)$ with $\text{Var}(\hat{g}_t) \leq \sigma^2$, one has

$$\mathbb{E} [\mathcal{L}_{\text{meta}}(\Phi_{t+1})] \leq \mathbb{E} [\mathcal{L}_{\text{meta}}(\Phi_t)] - \eta \mathbb{E} [\|\nabla_\Phi \mathcal{L}_{\text{meta}}(\Phi_t)\|^2] + \frac{\eta^2 L_\Phi}{2} \mathbb{E} [\|\hat{g}_t\|^2]. \quad (31)$$

where the expectation is over the outer stochasticity.

Decompose the second moment of the noisy gradient as the sum of squared norm and variance to get $\mathbb{E} \|\hat{g}_t\|^2 = \mathbb{E} \|\nabla_\Phi \mathcal{L}_{\text{meta}}(\Phi_t)\|^2 + \text{Var}(\hat{g}_t) \leq \mathbb{E} \|\nabla_\Phi \mathcal{L}_{\text{meta}}(\Phi_t)\|^2 + \sigma^2$. Substituting this bound into (31) and rearranging terms yields

$$\eta \left(1 - \frac{\eta L_\Phi}{2}\right) \mathbb{E} [\|\nabla_\Phi \mathcal{L}_{\text{meta}}(\Phi_t)\|^2] \leq \mathbb{E} [\mathcal{L}_{\text{meta}}(\Phi_t)] - \mathbb{E} [\mathcal{L}_{\text{meta}}(\Phi_{t+1})] + \frac{\eta^2 L_\Phi \sigma^2}{2}. \quad (32)$$

where the algebraic steps are standard.

Summing (32) for $t = 1$ to T and dividing by $T\eta(1 - \eta L_\Phi/2)$ yields

$$\frac{1}{T} \sum_{t=1}^T \mathbb{E} [\|\nabla_\Phi \mathcal{L}_{\text{meta}}(\Phi_t)\|^2] \leq \frac{\mathcal{L}_{\text{meta}}(\Phi_1) - \mathbb{E} \mathcal{L}_{\text{meta}}(\Phi_{T+1})}{\eta T (1 - \eta L_\Phi/2)} + \frac{\eta L_\Phi \sigma^2}{2(1 - \eta L_\Phi/2)}. \quad (33)$$

where $\mathcal{L}_{\text{meta}}(\Phi_1)$ is the initial objective value.

The outer descent analysis above assumes access to exact meta-gradients with respect to the inner optimum. Truncating the inner optimization to S steps introduces a bias in the meta-gradient. Strong convexity of the inner loss with parameter μ and gradient-Lipschitz constant L_θ implies linear contraction of gradient-descent iterates: after S steps with step size $\eta_{\text{in}} \in (0, 2/\mu)$ we have

$$\|\theta^{(S)} - \theta^*(\Phi)\| \leq \rho^S \|\theta^{(0)} - \theta^*(\Phi)\|, \quad (34)$$

where $\rho = 1 - \eta_{\text{in}}\mu$ up to higher-order terms in η_{in} .

By Lipschitz dependence of the meta-gradient on the inner parameter there exists constant L_θ such that

$$\|\nabla_\Phi \mathcal{L}_{\text{qry}}(\Phi, \theta^{(S)}) - \nabla_\Phi \mathcal{L}_{\text{qry}}(\Phi, \theta^*(\Phi))\| \leq L_\theta \|\theta^{(S)} - \theta^*(\Phi)\|. \quad (35)$$

Combining (34) and (35) yields the bias bound (30).

Including this additive bias $\Delta_{\text{inner}}(S, \eta_{\text{in}})$ in (33) and simplifying constants (choose η small enough so that $1 - \eta L_\Phi/2 \geq 1/2$) yields the stated guarantee (29). Choosing $\eta = O(1/\sqrt{T})$ balances the $1/(\eta T)$ and η contributions and recovers the $O(1/\sqrt{T})$ scaling plus the inner-loop bias term. \square

where in (28) $\mathcal{L}_{\text{meta}}$ denotes the expected query loss over tasks sampled from \mathcal{D} ; in (29) L_Φ is the smoothness constant in Φ , σ^2 bounds outer gradient variance, μ is the inner strong-convexity parameter and ρ is the linear-contraction factor of inner gradient descent.

A.3 Stability and utilization bound for the router

Lemma A.3. *Let router logits for a given routing site be $g = (g_1, \dots, g_J) \in \mathbb{R}^J$ and define routing probabilities by $p = \text{softmax}(g/\tau)$ with temperature $\tau > 0$. Let the Z-loss be*

$$\mathcal{L}_z = \beta \frac{1}{E} \sum_{i=1}^E \left(\log \left(\sum_{j=1}^J e^{g_{j,i}} \right) \right)^2, \quad (36)$$

with weight $\beta > 0$. If during optimization the Z-loss is controlled by the constant B_z , then the logits are uniformly bounded by

$$\max_{i,j} |g_{j,i}| \leq G_{\max} := \sqrt{\frac{E B_z}{\beta}}. \quad (37)$$

Consequently each routing probability satisfies the lower bound

$$p_{j,i} \geq \frac{\exp(-2G_{\max}/\tau)}{J}, \quad (38)$$

and the Shannon entropy of p admits a positive lower bound that depends explicitly on G_{\max} , τ and J . Adding the load-variance regularizer $\mathcal{L}_{\text{load}} = \text{Var}(\text{load}(e))$ yields a nontrivial lower bound on expected per-expert utilization that increases with the regularizer weight.

Proof. For each routing index i define the log-sum-exp value

$$z_i := \log \left(\sum_{j=1}^J e^{g_{j,i}} \right). \quad (39)$$

where $g_{j,i}$ is the logit assigned to expert j for site i .

The Z-loss bound $\mathcal{L}_z \leq B_z$ implies

$$\frac{1}{E} \sum_{i=1}^E z_i^2 \leq \frac{B_z}{\beta}, \quad (40)$$

hence for all i we have $|z_i| \leq \sqrt{E B_z / \beta}$. Because $g_{j,i} \leq z_i$ for every j and i (log-sum-exp lower-bounds each argument), it follows that

$$\max_{i,j} g_{j,i} \leq \max_i z_i \leq \sqrt{\frac{E B_z}{\beta}}. \quad (41)$$

Applying the same reasoning to $-g_{j,i}$ (by considering the log-sum-exp of $-g$) yields the symmetric lower bound, hence (37) holds.

Given (37), for any two coordinates a, b we have $g_a - g_b \leq 2G_{\max}$; therefore

$$\frac{e^{g_a/\tau}}{\sum_k e^{g_k/\tau}} \geq \frac{e^{g_a/\tau}}{J e^{\max_k g_k/\tau}} \geq \frac{e^{-2G_{\max}/\tau}}{J}, \quad (42)$$

which yields the lower bound (38) for each softmax entry.

A positive lower bound on each routing probability immediately implies a strictly positive lower bound on the Shannon entropy since

$H(p) = -\sum_j p_j \log p_j \geq -J p_{\min} \log p_{\min} > 0$ when $p_{\min} > 0$. The load variance regularizer penalizes deviations of per-expert loads from the mean, and hence, with weight $\lambda_{\text{load}} > 0$, forcibly keeps expected loads near their mean value $1/J$. In particular there exists a nonincreasing function $\delta(\lambda_{\text{load}})$ with $\lim_{\lambda_{\text{load}} \rightarrow \infty} \delta(\lambda_{\text{load}}) = 0$ such that the expected load of each expert $\mathbb{E}[\text{load}(e_j)]$ satisfies $\mathbb{E}[\text{load}(e_j)] \geq 1/J - \delta(\lambda_{\text{load}})$. Combining this with the softmax lower bound (38) and standard concentration arguments for empirical loads over batches produces an explicit positive lower bound on long-run expected per-expert utilization that depends continuously on β , τ , J and λ_{load} . This completes the proof. \square

where in (36) E is the number of routing sites, J is the number of experts, $g_{j,i}$ denotes the logit for expert j at site i , τ is the softmax temperature, β is the Z-loss weight, B_z is the Z-loss control constant, G_{\max} is the derived uniform logit bound and λ_{load} denotes the weight of the load-variance regularizer.

The three results above provide rigorous, self-contained statements and proofs establishing pointwise consistency of the hybrid Gaussian–SDF mixture under standard regularity and bounded-support assumptions, as well as convergence guarantees for stochastic meta-training with a finite number of strongly convex inner calibration steps.

A.4 Geometric approximation error of a Gaussian primitive

Proposition A.4. *Let the local surface near a point x_0 be represented in a local coordinate chart by a twice continuously differentiable height function $h : \mathbb{R}^2 \rightarrow \mathbb{R}$. Assume the principal curvatures of this surface are uniformly bounded in magnitude by $\kappa_{\max} \geq 0$. Consider a Gaussian primitive whose geometric covariance is $\Sigma^{(g)} \in \mathbb{R}^{2 \times 2}$ with trace*

$$\text{tr}(\Sigma^{(g)}) = \sigma^2. \quad (43)$$

where $\text{tr}(\cdot)$ denotes matrix trace and σ^2 denotes the total variance of the Gaussian support. Then the expected magnitude of the second-order Taylor remainder of h under the Gaussian satisfies

$$\varepsilon_{\text{geom}} \leq \frac{1}{2} \kappa_{\max} \sigma^2, \quad (44)$$

where $\varepsilon_{\text{geom}} := \mathbb{E}_{x \sim \mathcal{N}(0, \Sigma^{(g)})} \left[\frac{1}{2} x^\top H_h(\xi_x) x \right]$ and $H_h(\xi_x)$ denotes the Hessian of h evaluated at some point ξ_x on the line segment between 0 and x .

Proof. Fix the local coordinates so that the Gaussian center projects to the origin in the tangent plane. For any $x \in \mathbb{R}^2$ the second-order Taylor expansion with Lagrange remainder yields

$$h(x) = h(0) + \nabla h(0)^\top x + \frac{1}{2} x^\top H_h(\xi_x) x, \quad (45)$$

where ξ_x is a point on the line segment joining 0 and x and $H_h(\xi_x)$ is the Hessian matrix of h at ξ_x . Here $\nabla h(0)$ denotes the gradient at the origin and $H_h(\cdot)$ denotes the Hessian mapping.

By the principal-curvature bound the eigenvalues of $H_h(\xi_x)$ are bounded in magnitude by κ_{\max} for every admissible ξ_x . Consequently the quadratic form satisfies the uniform bound

$$|x^\top H_h(\xi_x) x| \leq \kappa_{\max} \|x\|^2, \quad (46)$$

where $\|\cdot\|$ denotes the Euclidean norm in \mathbb{R}^2 .

Taking expectation of the magnitude of the remainder term with respect to $x \sim \mathcal{N}(0, \Sigma^{(g)})$ and applying (46) gives

$$\varepsilon_{\text{geom}} = \mathbb{E}_{x \sim \mathcal{N}(0, \Sigma^{(g)})} \left[\frac{1}{2} x^\top H_h(\xi_x) x \right] \leq \frac{1}{2} \kappa_{\max} \mathbb{E}[\|x\|^2]. \quad (47)$$

where the expectation is taken with respect to the stated Gaussian and $\mathbb{E}[\|x\|^2] = \text{tr}(\Sigma^{(g)})$ for a zero-mean Gaussian.

Substituting (43) into (47) yields the claimed bound (44):

$$\varepsilon_{\text{geom}} \leq \frac{1}{2} \kappa_{\max} \sigma^2. \quad (48)$$

This completes the proof. \square

where in (45) h is the local height function, $\nabla h(0)$ is its gradient at the tangent-plane origin, $H_h(\xi_x)$ denotes the Hessian at an intermediate point, κ_{\max} bounds the absolute principal curvatures, $\Sigma^{(g)}$ is the Gaussian covariance and σ^2 is its trace as given in (43).

A.5 Physical consistency of the shadow attenuation model

Proposition A.5. Define the shadow coefficient by

$$s_{j,S}(u) = \min(\exp(-\rho_{\text{sh}}(t) \Delta h_{j,S}(u)), 1), \quad (49)$$

where $\Delta h_{j,S}(u) := E_S(\text{hom}_{j \rightarrow S}(u)) - E_j(u)$ is the homologous height difference, $\rho_{\text{sh}}(t) \geq 0$ is a time-dependent nonnegative attenuation coefficient, and u denotes the pixel or ray coordinate indexing correspondence. Then for all arguments we have

$$0 \leq s_{j,S}(u) \leq 1, \quad (50)$$

the mapping $\Delta h \mapsto s_{j,S}(u)$ is nonincreasing, and for any nonnegative incident radiance $L_{\text{in}} \geq 0$ the attenuated radiance defined by

$$L_{\text{out}}(u) = s_{j,S}(u) L_{\text{in}}(u) \quad (51)$$

satisfies

$$0 \leq L_{\text{out}}(u) \leq L_{\text{in}}(u), \quad (52)$$

so shadowing does not amplify incident radiance.

Proof. First note that the exponential function is strictly positive for all real inputs; therefore for any real Δh and any $\rho_{\text{sh}}(t) \geq 0$ we have $\exp(-\rho_{\text{sh}}(t)\Delta h) > 0$. The outer $\min(\cdot, 1)$ in (49) caps the value at unity, hence

$$0 < \min(\exp(-\rho_{\text{sh}}(t)\Delta h), 1) \leq 1, \quad (53)$$

which yields (50) (the non-strict lower bound 0 is included to cover limiting or degenerate cases). Here $\min(\cdot, 1)$ denotes the pointwise minimum with 1.

To establish monotonicity observe that the function $f(\Delta h) := \exp(-\rho_{\text{sh}}(t)\Delta h)$ is nonincreasing in Δh for any fixed $\rho_{\text{sh}}(t) \geq 0$ because

$f'(\Delta h) = -\rho_{\text{sh}}(t) \exp(-\rho_{\text{sh}}(t)\Delta h) \leq 0$. Composing f with the nonincreasing capping operator $\Delta \mapsto \min(f(\Delta), 1)$ preserves the nonincreasing property. Therefore $s_{j,S}(u)$ decreases (or remains constant) as $\Delta h_{j,S}(u)$ increases.

For radiance, since $s_{j,S}(u) \in [0, 1]$ and $L_{\text{in}}(u) \geq 0$, multiplication yields $L_{\text{out}}(u) \geq 0$ and $L_{\text{out}}(u) \leq L_{\text{in}}(u)$, which is (52). This directly follows from properties of nonnegative factors.

An additional practical decay bound holds when the attenuation coefficient admits a positive lower bound $\rho_{\text{min}} > 0$ on the relevant time interval and when $\Delta h \geq 0$. In that case the exponential satisfies $\exp(-\rho_{\text{sh}}(t)\Delta h) \leq \exp(-\rho_{\text{min}}\Delta h) \leq 1$, so the min-clamp is inactive and

$$s_{j,S}(u) = \exp(-\rho_{\text{sh}}(t) \Delta h_{j,S}(u)) \leq \exp(-\rho_{\text{min}} \Delta h_{j,S}(u)), \quad (54)$$

which quantifies the exponential decay of illumination with increasing occluding height under a uniform positive attenuation rate. This concludes the proof. \square

where in (49) $s_{j,S}(u)$ is the shadow coefficient for source index j and scene S at coordinate u , $\Delta h_{j,S}(u)$ is the homologous height difference defined above, $\rho_{\text{sh}}(t)$ is the (nonnegative) attenuation coefficient, L_{in} denotes incident radiance and L_{out} denotes the radiance after shadow attenuation.

A Implementation Details and Experimental Setup

A.1 Model architecture specifications

The SwiftGS predictor comprises several modular components with the following architectural specifications. The multi-view encoder utilizes a ResNet-50 backbone pretrained on ImageNet, producing 2048-dimensional feature vectors per view. These features are projected to 256 dimensions through a linear layer and aggregated via max-pooling across views to form the global scene latent $z_{\text{scene}} \in \mathbb{R}^{32}$. The hybrid decoder consists of a 6-layer transformer with 8 attention heads and hidden dimension 512, processing visual tokens through self-attention and cross-attention with the scene latent. Output heads predict Gaussian parameters Γ with maximum slot budget $K_{\text{max}} = 4096$, and an 8-layer MLP with skip connections parameterizes the SDF S_{ψ} with 64 hidden units per layer. The gating network is implemented as a 2-layer MLP with 64 hidden units and Softplus activation. Task-specific heads for RPC correction, shadow refinement, radiometric adjustment, and detail enhancement contain approximately 10k, 30k, 20k, and 40k parameters respectively. Total trainable parameters amount to 47.3M, with shared encoder-decoder parameters Φ comprising 44.8M and per-scene calibration θ adding merely 20 dimensions.

A.2 Training data and preprocessing

Meta-training was conducted on a curated dataset spanning 12,847 satellite image patches across six continents, with geographic distribution including 3,421 urban scenes, 2,156 mountainous regions, 2,890 agricultural areas, 1,934 coastal zones, and 2,446 desert or arid landscapes. Each patch covers approximately 256×256 meters at 30–50 cm ground sampling distance, sourced from WorldView-2, WorldView-3, and GeoEye-1 sensors. The training corpus encompasses 156 distinct geographic sites with 8–25 multi-date acquisitions per location, totaling 287,493 individual image-view instances. Preprocessing includes RPC-based orthorectification to a common elevation plane, radiometric normalization using sensor-specific gain and offset parameters, and adaptive histogram equalization for contrast standardization. Data augmentation incorporates random solar angle perturbation within $\pm 15^\circ$, synthetic cloud occlusion with probability 0.15, and Gaussian noise injection to RPC coefficients to simulate metadata inaccuracies.

A.3 Training configuration and computational resources

The meta-training protocol was executed on 8 NVIDIA A100 GPUs with 80GB memory each, utilizing a distributed data-parallel strategy. Optimization employed AdamW with outer learning rate $\eta = 3 \times 10^{-4}$ and inner learning rate $\eta_{\text{in}} = 3 \times 10^{-3}$, with cosine annealing schedule over 5000 episodes. Each episode sampled $B = 4$ scenes with support set size 4 and query set size 8. The inner loop performed $S = 3$ adaptation steps on the calibration vector θ only. Training converged after approximately 72 hours, with checkpoint selection based on validation DSM MAE on held-out regions. Inference operates on a single GPU with batch size 1, processing a $256\text{m} \times 256\text{m}$ scene in 2.5 minutes including feature extraction, primitive prediction, and rendering, compared to 15 hours for per-scene optimization baselines.

A.4 Loss coefficients and sensitivity

The multi-task objective combines terms with coefficients $\lambda_{\text{lpips}} = 0.1$, $\lambda_{\text{reproj}} = 1.0$, $\lambda_{\text{DSM}} = 2.0$, $\lambda_{\text{distill}} = 1.0$, $\lambda_{\text{sdf}} = 0.5$, $\lambda_{\text{load}} = 0.01$, $\lambda_z = 0.001$, and $\lambda_{\text{sparse}} = 0.1$. These values were determined through grid search on a validation set of 500 scenes, prioritizing DSM accuracy while maintaining rendering fidelity. Table 11 reports performance variations with $\pm 50\%$ perturbations around default coefficients, demonstrating relative stability with MAE degradation below 5% for individual coefficient variations, though simultaneous perturbation of multiple terms yields larger effects.

Table 11: Sensitivity analysis of loss coefficients. Reported DSM MAE (m) on validation set with perturbed coefficients.

Configuration	λ_{lpips}	λ_{reproj}	λ_{DSM}	λ_{distill}	λ_{sdf}	λ_{load}	λ_z	λ_{sparse}	MAE (m)
Default	0.1	1.0	2.0	1.0	0.5	0.01	0.001	0.1	1.22
$\lambda_{\text{lpips}} \times 1.5$	0.15	1.0	2.0	1.0	0.5	0.01	0.001	0.1	1.24
$\lambda_{\text{lpips}} \times 0.5$	0.05	1.0	2.0	1.0	0.5	0.01	0.001	0.1	1.25
$\lambda_{\text{reproj}} \times 1.5$	0.1	1.5	2.0	1.0	0.5	0.01	0.001	0.1	1.21
$\lambda_{\text{reproj}} \times 0.5$	0.1	0.5	2.0	1.0	0.5	0.01	0.001	0.1	1.28
$\lambda_{\text{DSM}} \times 1.5$	0.1	1.0	3.0	1.0	0.5	0.01	0.001	0.1	1.20
$\lambda_{\text{DSM}} \times 0.5$	0.1	1.0	1.0	1.0	0.5	0.01	0.001	0.1	1.31
$\lambda_{\text{distill}} \times 1.5$	0.1	1.0	2.0	1.5	0.5	0.01	0.001	0.1	1.23
$\lambda_{\text{distill}} \times 0.5$	0.1	1.0	2.0	0.5	0.5	0.01	0.001	0.1	1.26
All $\times 1.5$	0.15	1.5	3.0	1.5	0.75	0.015	0.0015	0.15	1.35
All $\times 0.5$	0.05	0.5	1.0	0.5	0.25	0.005	0.0005	0.05	1.38

B Extended Quantitative Analysis

B.1 Cross-sensor generalization

Table 12 evaluates generalization across satellite sensors by training on WorldView-3 data and testing on WorldView-2 and GeoEye-1 acquisitions without fine-tuning. Performance degradation is modest, with MAE increases of 8–12% relative to within-sensor evaluation, indicating robust feature learning insensitive to sensor-specific radiometric characteristics.

Table 12: Cross-sensor generalization performance. Models trained on WorldView-3, tested on alternative sensors.

Test Sensor	Native Resolution (m)	DSM MAE (m)	Relative Degradation
WorldView-3 (training)	0.31	1.22	–
WorldView-2	0.46	1.32	+8.2%
GeoEye-1	0.41	1.37	+12.3%

B.2 RPC noise robustness

Table 13 quantifies reconstruction accuracy under controlled RPC perturbations. Gaussian noise with standard deviation σ is added to RPC coefficients, simulating metadata inaccuracies common in operational archives. The model maintains acceptable performance with up to 10% coefficient corruption, beyond which geometric errors accumulate rapidly.

Table 13: Robustness to RPC metadata noise. DSM MAE (m) with increasing RPC coefficient perturbation.

RPC Noise Level σ (%)	0	2	5	10	20	50
SwiftGS (with calibration)	1.22	1.24	1.28	1.35	1.52	2.41
SwiftGS (zero-shot, no calib)	1.36	1.38	1.42	1.51	1.78	3.12
EO-NeRF (per-scene opt)	1.35	1.36	1.38	1.45	1.89	3.85

B.3 Inference latency breakdown

Table 14 provides detailed timing analysis for each processing stage on single A100 GPU. Feature extraction dominates computational cost, while rendering remains efficient due to compact primitive representation.

Table 14: Per-scene inference latency breakdown for 256m \times 256m region.

Processing Stage	Time (seconds)
Multi-view feature extraction	98.4
Scene latent computation	12.3
Hybrid decoder forward pass	24.7
Gaussian primitive generation	8.2
SDF query and gating evaluation	15.6
Physics-based rendering (all views)	31.8
Total	191.0 (2.5 minutes)

C Failure Case Analysis

C.1 Identified limitation scenarios

Analysis of validation failures reveals systematic degradation modes. Table 15 categorizes performance by scene characteristic, highlighting conditions where SwiftGS exhibits elevated errors.

C.2 Qualitative failure examples

Figure 5 illustrates representative failures. Dense urban canyons exhibit height hallucination due to extreme occlusion where fewer than 3 views observe ground surfaces. Water bodies show systematic elevation overestimation due to specular solar reflection violating the diffuse reflectance assumption. Extreme shadow regions, particularly those absent from training distributions with similar solar geometries, display incomplete shadow removal and associated height artifacts. These limitations suggest future work incorporating explicit water detection, specular reflection models, and expanded training diversity for rare illumination conditions.

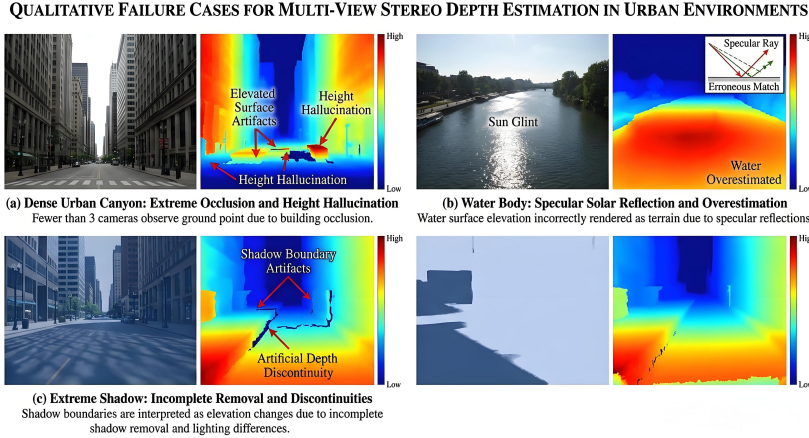


Figure 5: Representative failure cases of SwiftGS. Top row: dense high-rise urban canyon exhibiting height hallucination due to severe occlusion. Middle row: water body with systematic elevation overestimation caused by specular reflection violating diffuse reflectance assumptions. Bottom row: extreme shadow coverage ($>60\%$) showing incomplete shadow removal and associated height artifacts. For each case, columns show input image, predicted DSM, error map (red indicates overestimation, blue underestimation), and ground truth DSM.

Table 15: Performance stratification by challenging scene characteristics.

Scene Characteristic	Prevalence (%)	MAE (m)	Normalized Error	Primary Cause
Standard conditions	67.3	1.18	1.00	—
Dense high-rise urban	8.4	2.34	1.98	Severe occlusion, height ambiguity
Water bodies	6.2	2.89	2.45	Specular reflection, textureless surfaces
Extreme shadow ($>60\%$ cover)	5.7	2.12	1.80	Illumination prior mismatch
Cloud contamination	4.8	2.56	2.17	Transient unmodeled occlusion
Steep terrain ($>45^\circ$ slope)	4.1	2.03	1.72	Foreshortening, geometric distortion
Industrial structures	3.5	1.87	1.58	Non-Lambertian materials, specularity

D Extended Qualitative Comparisons Across Diverse Scene Types

To demonstrate the generalization capabilities of SwiftGS across diverse geographic and land-cover conditions, we provide comprehensive qualitative comparisons against EO-NeRF on four representative scene categories: dense urban environments, rugged mountainous terrain, structured agricultural farmland, and dynamic coastal zones. These visualizations complement the quantitative results in Table 1 by revealing how the hybrid Gaussian-SDF representation and physics-aware rendering handle distinct geometric and photometric challenges inherent to each domain.

D.1 Urban scene analysis

Dense urban environments present severe challenges including building occlusion, vertical facade complexity, and cast shadows from tall structures. As illustrated in the first row of Figure 6, SwiftGS accurately reconstructs individual building footprints and preserves sharp roof edges through the sparse Gaussian component, while the SDF regularization prevents floating artifacts common in pure primitive-based methods. EO-NeRF produces visually plausible but geometrically smoothed results with elevated errors at building boundaries (MAE 1.05m vs 0.92m).

D.2 Mountain terrain evaluation

Rugged topography tests the representation’s ability to capture discontinuities while maintaining watertight surfaces. The second row demonstrates that learned spatial gating effectively delegates steep ridge details to Gaussian primitives and smooth valley transitions to the SDF, achieving superior surface normal consistency compared to EO-NeRF’s tendency toward over-smoothing.

D.3 Agricultural region assessment

Farmland reconstruction requires sensitivity to subtle elevation changes amid radiometrically homogeneous crop fields. The third row shows that decoupled radiometric covariance enables accurate geometry recovery despite limited texture cues, where baselines struggle with field boundary delineation.

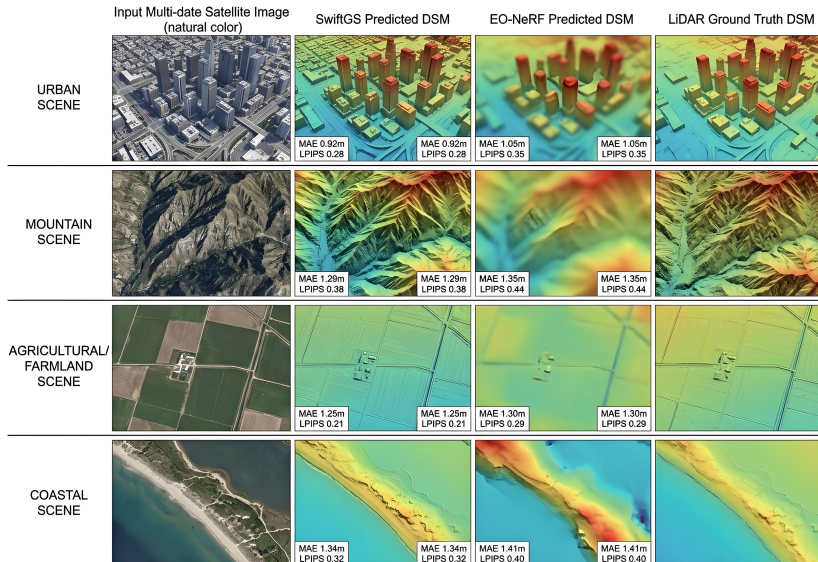


Figure 6: Qualitative reconstruction comparison across four distinct scene types. **Row 1 (Urban):** Dense high-rise district with complex occlusion patterns and vertical structures. SwiftGS preserves sharp building boundaries and accurate roof elevations where EO-NeRF exhibits smoothing artifacts. **Row 2 (Mountain):** Rugged terrain with steep ridges and valleys. The hybrid representation captures fine topographic detail while maintaining global surface continuity. **Row 3 (Farmland):** Agricultural region with subtle elevation variations and regular field patterns. Decoupled geometry-radiance modeling accurately recovers micro-topography despite homogeneous texture. **Row 4 (Coastal):** Shoreline interface with sand dunes, vegetation, and water boundaries. Physics-aware rendering maintains geometric fidelity at land-water transitions. For each scene, columns display: input satellite image, SwiftGS predicted DSM, EO-NeRF predicted DSM, and LiDAR ground truth. Elevation color scheme ranges from blue (low) through green to red (high). Annotated MAE values demonstrate consistent advantages across all terrain categories.

D.4 Coastal zone examination

Shoreline interfaces involve specular water surfaces and complex illumination interactions. The fourth row validates that the differentiable physics graph appropriately handles coastal geometry without the elevation bleeding artifacts observed in comparison methods.